Jurnal Elektronika dan Telekomunikasi (JET), Vol. 25, No. 2, December 2025, pp. 126- 140
Accredited by KEMDIKBUDRISTEK, Decree No: **158/E/KPT/2021**
doi: 10.55981/jet.757

Phase-Sensitive Radar Using ADALM-Pluto SDR and Cantenna for Sub-Millimeter Displacement Measurement

Eril Mozef*, Ridho Shofwan Rasyid, Enceng Sulaeman, Tiyo Rizky Mulyana, Fahrizal Al Farik, Thaskia Qolbi Junjunan

Department of Electrical Engineering
Politeknik Negeri Bandung
Jl. Geger Kalong Hilir, Ds Ciwaruga
Bandung, Indonesia

Abstract

The capability of phase-sensitive radar to detect sub-millimeter displacement has been widely demonstrated, enabling a range of applications such as structural vibration monitoring, human vital-sign detection, gesture sensing, and precision motion tracking. In these domains, particularly in non-contact human respiratory monitoring, conventional phase-sensitive radar systems offer key advantages, including high phase stability, robust performance under non-ideal lighting or environmental conditions, and the ability to operate without physical contact. These strengths make them effective for capturing small periodic chest movements required for accurate respiratory assessment. However, conventional hardware implementations often suffer from limited flexibility, higher development cost, and increased design complexity. These constraints motivate the shift toward software-defined radio (SDR) solutions, which provide reconfigurability, simplified prototyping, and significantly lower cost while retaining the essential phase-sensitive capabilities. This motivation forms the basis of the present research. This study realizes a phase-sensitive radar using an ADALM-Pluto SDR operating at 2.45 GHz with a cantenna antenna configuration. Compared with previous SDR-based works that focus primarily on Doppler vital-sign extraction or require more elaborate RF front-ends, the proposed system emphasizes displacement-resolution enhancement through careful phase processing while maintaining minimal hardware complexity. The combination of a compact SDR platform, simple antenna structure, and optimized signal processing pipeline yields a practical and accessible radar prototype. Experimental results demonstrate that the proposed system achieves a displacement resolution of 0.5 mm, meeting the requirements for developing a reliable respiratory-monitoring application and confirming the suitability of SDR-based phase-sensitive radar for low-cost biomedical sensing.

Keywords: phase-sensitive radar, software-defined radio, sub-millimeter-displacement measurement, cantenna directional antenna, non-contact human respiratory monitoring.

I. INTRODUCTION

Phase-sensitive radar systems are capable of detecting minute motion, often down to the sub-millimeter scale, by precisely tracking phase variations of reflected electromagnetic waves. This exceptional displacement sensitivity is crucial for a wide range of non-contact sensing applications, including vital-sign monitoring, sleep monitoring, gesture recognition, fall detection, and presence detection [1], [2], [3]. Among these, non-contact respiration monitoring has received significant attention because chest-wall motion during breathing typically ranges from a few millimeters down to sub-millimeter amplitudes during shallow breathing. Such small biomechanical movements lie well within the measurement capability of phase-sensitive radar, enabling continuous monitoring without requiring physical sensors attached to the subject, a major advantage for comfort, hygiene, long-term observation, and clinical feasibility [1].

Conventional phase-sensitive radar implementations offer several advantages in the context of vital-sign detection. Their dedicated RF front-ends typically deliver high phase stability, low phase noise, and well-characterized quadrature demodulation, allowing accurate retrieval of both respiratory and heartbeat micro-motions [1], [2]. High-frequency CW radar systems (e.g., 24 GHz, 60 GHz, 77 GHz, and 94 GHz) have demonstrated reliable monitoring of breathing patterns even under non-ideal conditions such as clutter or multipath reflections [3]. In non-contact respiratory monitoring, these traditional radars often achieve high signal fidelity due to stable analog mixing chains and optimized RF paths [1], [3].

However, despite their strong performance, conventional radars suffer from several critical limitations. They generally require complex analog RF design, tight component tolerances, precise calibration, and specialized hardware. These factors contribute to

* Corresponding Author.
Email: emozef@polban.ac.id
Received: June 26, 2025 ; Revised : November 17, 2025
Accepted: December 09, 2025 ; Published: December 31, 2025

high cost, limited flexibility, and poor scalability. Furthermore, tuning radar parameters (carrier frequency, LO power, IF bandwidth) typically requires hardware modifications or redesigns, making them impractical for rapid prototyping or deployment across diverse environments, challenges that are particularly important for real-world non-contact respiratory monitoring [2], [3]. These limitations motivate the need for a more adaptable and lower-cost alternative.

Software-Defined Radio (SDR) platforms provide such an alternative by enabling most radar signal-processing operations, modulation, demodulation, filtering, and spectral shaping, to be implemented entirely in software. This results in greatly enhanced flexibility, rapid reconfigurability, and significantly lower cost. Recent works have shown that SDR-based radars can effectively measure human respiration, detect abnormal breathing patterns, and even track multiple subjects simultaneously [4], [5], [6]. For example, SDR-based Doppler radar has been used to perform real-time breathing detection with I/Q demodulation [4], while other studies demonstrate SDR-assisted machine-learning classification of respiratory anomalies [5] and multi-person respiratory tracking using software-based phase analysis [6]. These works confirm that SDR-based radar is a practical and powerful option for non-contact respiratory monitoring.

Motivated by these advantages, the present research realizes a phase-sensitive radar system using the ADALM-Pluto SDR, operating at 2.45 GHz and equipped with a cantenna directional antenna.

- ADALM-Pluto is chosen for its affordability, full-duplex I/Q transceiver, and software-controlled RF chain, making it ideal for flexible radar prototyping.
- The 2.45 GHz ISM band provides license-free operation and a wavelength (~12.24 cm) suitable for detecting sub-millimeter chest-wall displacement through phase modulation.
- The cantenna offers low-cost construction, ease of fabrication, and stable directional gain, improving SNR for phase-sensitive operation.

This study is a continuation of previous work that has been registered with the Directorate General of Intellectual Property [7].

A survey of existing literature shows that, although SDR-based radar for vital-sign monitoring is well explored, the combination of ADALM-Pluto, operation at 2.45 GHz, phase-sensitive CW architecture, and cantenna antennas specifically for non-contact respiratory monitoring is rarely reported.

The proposed system therefore provides:

- A novel low-cost phase-sensitive radar architecture.
- A flexible SDR-based platform suitable for rapid respiration-sensing research.
- A simple, replicable antenna solution tailored for non-contact monitoring scenarios.

This contribution addresses the limitations of conventional radars and enables practical, accessible experimentation for real-world non-contact respiratory monitoring applications.

II. METHOD

A. Theoretical Background

In the following section, the block diagram of the proposed phase-sensitive radar (Figure 1) is explained, along with the output equations of each block, leading to the derivation of the phase value as a function of distance.

1) Assumptions and Notation

- t = time.
- $\omega = 2\pi f$.
- A_x = amplitude of signal x.
- ϕ_x = phase offset of signal x.
- $s_{gen}(t)$ = sinusoidal generator output (base tone).
- $LO(t)$ = local oscillator.
- Mixer multiplication is ideal multiplication; bandpass or lowpass filtering after mixing is shown explicitly when needed.
- α = complex scattering coefficient of the target (amplitude attenuation and phase shift).
- τ = two-way delay from transmit to target back to receive (range→time).
- $n_i(t)$ = noise at receiver i(additive).
- After downconversion and LPF we represent complex baseband signals by capital letters (e.g., $R_1(t)$, $R_2(t)$).
- LPF $\{\cdot\}$ means ideal low-pass filtering that removes high-frequency (sum) terms and keeps the baseband component.
- $\angle\{\cdot\}$ deniotesmeans complex argument (phase).

2) Output of the Sinusoidal Generator (transmit base tone)

$$s_{gen}(t) = A_g \cos(\omega_g t + \phi_g) \quad (1)$$

A real sinusoidal tone produced by the signal generator. This is the low-frequency/baseband tone that will be upconverted by Mixer 1.

3) Output of the Local Oscillator (LO)

$$LO(t) = A_{LO} \cos(\omega_{LO} t + \phi_{LO}) \quad (2)$$

A stable sinusoidal reference used for frequency translation (both upconversion and downconversion). Its frequency ω_{LO} defines the RF carrier when mixed with the generator tone.

4) Output of Mixer 1 (upconversion), raw mixer output

$$v_{mix1}(t) = s_{gen}(t) \cdot LO(t) = A_g A_{LO} \cos(\omega_g t + \phi_g) \cos(\omega_{LO} t + \phi_{LO}) \quad (3)$$

Using the trigonometry identity (sum/difference),

$$v_{mix1}(t) = \frac{A_g A_{LO}}{2} [\cos((\omega_g + \omega_{LO})t + \phi_g + \phi_{LO}) + \cos((\omega_g - \omega_{LO})t + \phi_g - \phi_{LO})] \quad (4)$$

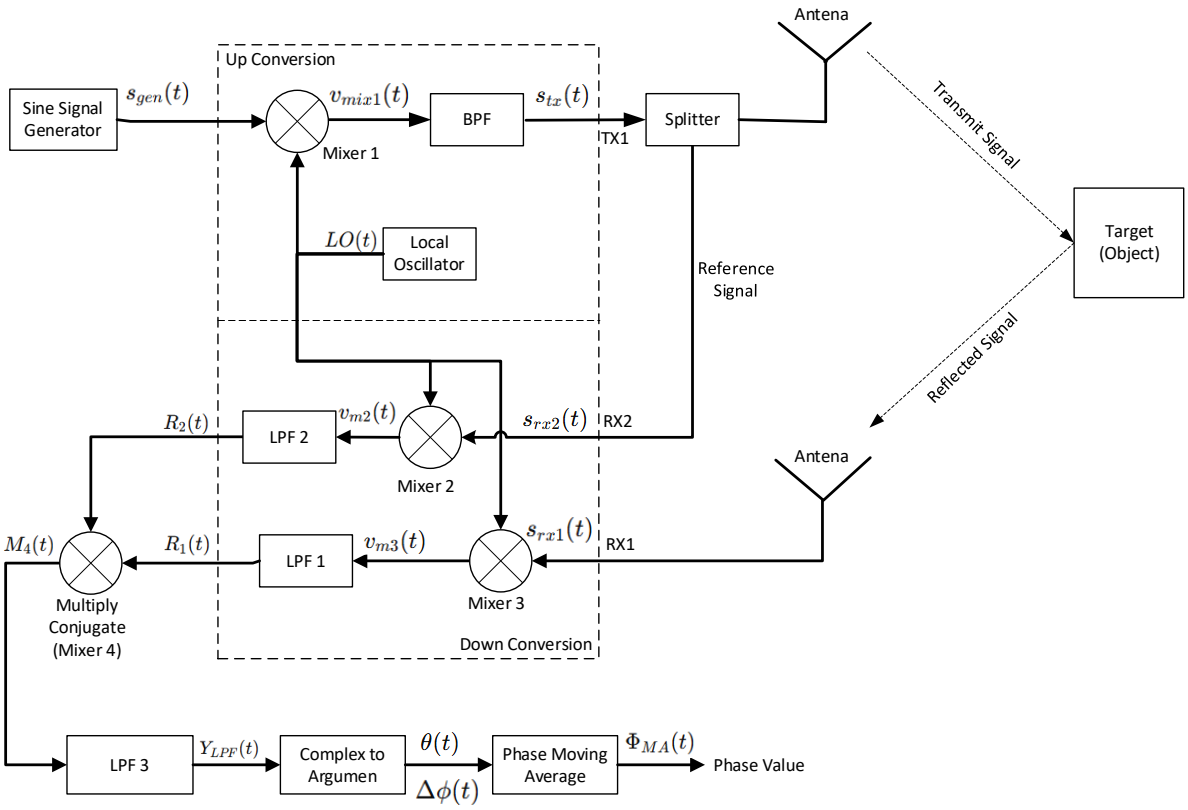

Figure 1. Proposed radar principle and equations.

After RF bandpass filtering (select the upper sideband/carrier), transmit signal,

$$s_{tx}(t) \approx \frac{A_g A_{LO}}{2} \cos\left((\omega_c)t + \phi_{tx}\right) \quad (5)$$

with $\omega_c = \omega_g + \omega_{LO}, \qquad \phi_{tx} = \phi_g + \phi_{LO}$

Mixer 1 multiplies generator and LO, producing sum and difference frequency components. The RF transmit path filters and selects the desired carrier component (usually the sum, the transmit carrier ω_c). That filtered waveform is sent to the antenna.

5) Input to RX2 (reference receive port, direct-coupled transmit reference)

$$s_{rx2}(t) = \beta\, s_{tx}(t) + n_2(t) \quad (6)$$

or, substituting s_{tx},

$$s_{rx2}(t) = \beta \frac{A_g A_{LO}}{2} \cos\left(\omega_c t + \phi_{tx}\right) + n_2(t) \quad (7)$$

where β models coupling/attenuation into RX2.

RX2 sees a copy (reference) of the transmitted signal (through coupling or a directional coupler). This path provides a phase/time reference against which echoes are compared.

6) Input to RX1 (received echo from target)

$$s_{rx1}(t) = \alpha\, s_{tx}(t - \tau) + n_1(t) \quad (8)$$

or

$$s_{rx1}(t) = \alpha \frac{A_g A_{LO}}{2} \cos\left(\omega_c(t - \tau) + \phi_{tx}\right) + n_1(t) \quad (9)$$

with complex $\alpha = |\,\alpha\,|\, e^{j\phi_\alpha}$ if expressed in complex form.

RX1 receives the reflected echo: a delayed, attenuated, and phase-shifted copy of the transmitted carrier plus local noise.

7) Output of Mixer2 (downconversion of RX2, the reference)

$$v_{m2}(t) = s_{rx2}(t) \cdot LO(t) \quad (10)$$

Substituting and keeping baseband after LPF (ideal downconversion to complex baseband),

$$R_2(t) \equiv \text{LPF}\,\{v_{m2}(t)\} \approx C_2\, e^{j(\phi_{ref}(t))} + \eta_2(t) \quad (11)$$

More explicit form (assuming an analytic representation of s_{rx2}),

$$R_2(t) \approx \tilde{\beta}\, e^{j(\omega_c t + \phi_{tx})} \cdot e^{-j(\omega_{LO} t + \phi_{LO})} \quad (12)$$

after LPF,

$$\tilde{A}_2\, e^{j(\Delta\omega\, t + \Delta\phi_2)} + \eta_2(t) \quad (13)$$

if LO is chosen so $\omega_c - \omega_{LO} = 0$ then after LPF,

$$R_2(t) \approx \tilde{A}_2 e^{j\phi_2} + \eta_2(t) \quad (14)$$

Mixer 2 multiplies the reference RX2 signal by the LO. After low-pass filtering the high-frequency terms, we obtain a complex baseband reference $R_2(t)$ whose

phase tracks the transmitted carrier phase (and LO phase). η_2 denotes residual noise/error.

8) Output of Mixer3 (downconversion of RX1, the echo)

$$v_{m3}(t) = s_{rx1}(t) \cdot LO(t) \quad (15)$$

After LPF (keeping the desired baseband component),

$$R_1(t) \equiv \text{LPF}\{v_{m3}(t)\} \approx \tilde{A}_1\, e^{j(\phi_1(t))} + \eta_1(t) \quad (16)$$

with explicit relation to delay,

$$R_1(t) \approx \tilde{A}_1 e^{j(-\omega_c\tau+\phi_{tx}+\phi_\alpha)} + \eta_1(t) \quad (17)$$

(so, the echo baseband phase contains the round-trip delay term $-\omega_c\tau$).

Mixer 3 down converts the received echo. After LPF we get a complex baseband $R_1(t)$ whose phase contains the target delay (hence range) and any phase modulation caused by movement.

9) Output of Multiply Conjugate (Mixer4)

$$M_4(t) = R_2(t) \cdot R_1^*(t) \quad (18)$$

If we write,

$$R_2(t) = A_2 e^{j\phi_2(t)} \text{and } R_1(t) = A_1 e^{j\phi_1(t)} \quad (19)$$

(neglecting noise) then,

$$M_4(t) = A_2 A_1 e^{j(\phi_2(t)-\phi_1(t))} \quad (20)$$

Multiplying the reference by the complex conjugate of the echo cancels common phase terms and yields a complex number whose phase equals the phase difference between reference and echo,

$$\Delta\phi(t) = \phi_2(t) - \phi_1(t) \quad (21)$$

this is the core phase-sensitive measurement.

10) Output of the Low Pass Filter (LPF) after Multiply Conjugate

$$Y_{LPF}(t) = \text{LPF}\{M_4(t)\} \quad (22)$$

If $M_4(t)$contains fast residual fluctuations, LPF smooths them; so approximately,

$$Y_{LPF}(t) \approx A_{12}(t)\, e^{j\Delta\phi(t)} \quad (23)$$

(slowly varying amplitude and phase).

LPF removes residual high-frequency components and noise, leaving a smoothly varying complex phasor whose argument is the phase difference between TX reference and echo. This improves SNR and makes phase extraction easier.

11) Output of Complex to Argument (phase extraction)

$$\theta(t) = \angle(Y_{LPF}(t)) = \arg(Y_{LPF}(t)) \quad (24)$$

So, if $Y_{LPF}(t) = A_{12}(t)e^{j\Delta\phi(t)}$, then

$$\theta(t) = \Delta\phi(t) (\text{mod } 2\pi) \quad (25)$$

Convert the complex phasor into a real phase time series. This is the instantaneous phase difference measurement (wrapped to $[-\pi, \pi]$ typically).

12) Output of Phase Moving Average (smoothing/tracking)

Simple moving average over N samples with sampling interval T_s,

$$\Phi_{MA}(t) = \frac{1}{N}\sum_{k=0}^{N-1} \quad \theta(t - kT_s) \quad (26)$$

if continuous smoothing is desired, an exponential smoother can be used,

$$\Phi_{MA}(t) = (1-\gamma)\Phi_{MA}(t-\Delta t) + \gamma\,\theta(t), 0 < \gamma \leq 1 \quad (27)$$

This stage reduces phase noise and produces a more stable phase estimate over time. The averaged phase can be used to detect small phase changes caused by micro-motion (e.g., breathing, vibration). Note: because phase is wrapped, phase averaging must be implemented as vector (complex) averaging or using phase-unwrapping to avoid wrapping artifacts (i.e., average the complex phasors $e^{j\theta(t)}$ and then take the argument).

13) Relationship Between Phase and Distance

From the previous discussion,

- Transmit signal after the BPF,

$$s_{tx}(t) = A_t \cos(\omega_c t + \phi_{tx}) \quad (28)$$

- Reflected signal received at RX1,

$$s_{rx1}(t) = \alpha\, A_t \cos[\omega_c(t-\tau) + \phi_{tx}] \quad (29)$$

with $\tau = \frac{2d}{c}$ (two-way delay (double distance))

Use a complex representation (to simplify phase analysis),

$$s_{tx}(t) = A_t e^{j\omega_c t}$$
$$s_{rx1}(t) = \alpha A_t e^{j\omega_c(t-\tau)} = \alpha A_t e^{j(\omega_c t - \omega_c\tau)} \quad (30)$$

when the RX1 signal is mixed with the LO (with the same frequency as the TX signal, ω_c) and filtered by the LPF,

$$R_1(t) = \text{LPF}\{s_{rx1}(t) \cdot e^{-j\omega_c t}\} = \alpha A_t e^{-j\omega_c\tau} \quad (31)$$

thus, the baseband phase is (32),

$$\phi_1 = -\omega_c\tau \quad (32)$$

if delay $\tau = \frac{2d}{c}$

$$\phi_1 = -\omega_c(\frac{2d}{c}) \quad (33)$$

since $\omega_c = 2\pi f_{\text{Tx}}$, then,

$$\phi_1 = -\frac{4\pi f_{\text{Tx}} d}{c} \quad (34)$$

then the equation becomes (35),

$$\phi = -\frac{4\pi f_{\mathrm{Tx}} d}{c} \quad (35)$$

where ϕ is the phase difference, f_{Tx} is the carrier frequency, d is the distance, and c is the speed of light.

If $\frac{f_{\mathrm{Tx}}}{c} = \frac{1}{\lambda}$, then (35) can be written as,

$$\Delta\phi(d) = -\frac{4\pi}{\lambda}\, d \quad (36)$$

(36) can also be written as,

$$\Delta\phi(d) = \frac{4\pi}{\lambda}\, d \quad (37)$$

The reason the '–' sign appears in (36) is because, for the downconversion process to baseband, $e^{-j\omega_c t}$is used (31). If we want to upconvert to the carrier frequency, then $e^{+j\omega_c t}$is used, resulting in the '+' sign in (37).

B. System Overview

Figure 2 illustrates the system overview. It includes a computer running the GNU Radio application, radar hardware, and two cantennas: one for transmitting the signal and the other for receiving it. The proposed hardware functions as both transmitter and receiver. The reflected signal is processed and sent to the computer via a USB 2.0 connector for display.

C. Radar Hardware Design and Implementation

The radar hardware system is a unit that combines the reference signal at RX2 and the reflected signal from the antenna at RX1 using a splitter, processes them in the SDR device, and then visualizes the result as plots on the monitor screen.

1) Implementation

Figure 3 (a) shows the wiring diagram of the radar hardware system. Figure 3 (b) shows its implementation inside a casing, which contains an ADALM-Pluto SDR device (Analog Devices), a splitter, antenna connectors, a USB socket, an ON–OFF switch, a PSU, a power supply unit, a step-down converter, and a cooling fan.

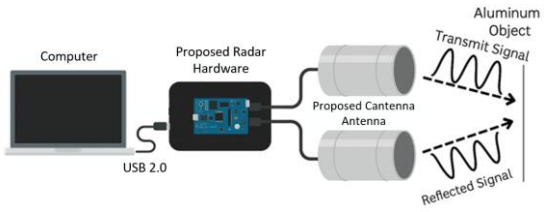

Figure 2. System overview.

The SDR device used is the 2-port version of the ADALM-Pluto (Figure 4 (a)). This version only provides two ports, TX1 and RX1, whereas an additional RX port (RX2) is required. In fact, this port already exists internally but is not exposed. To make it available, a wire must be soldered to the RX2 PCB trace, as shown in Figure 4 (b). Next, the MIMO (Multiple-Input Multiple-Output) mode must be enabled. This can be done by visiting the official Analog Devices website and updating the firmware to the latest version that supports MIMO (at least v0.32).

D. Cantenna Design and Implementation

A cantenna is a simple cylindrical waveguide antenna, typically made from a metal can, that provides directional gain and ease of fabrication for radio-frequency application. Its stable phase response and narrow beamwidth make it useful in phase-sensitive radar systems, where small variations in target distance are inferred from phase changes in the received signal [8]. By aligning the cantenna's radiation pattern with the radar's transmit–receive path, the system can achieve enhanced sensitivity to micro-motions and improved signal-to-noise ratio, making it suitable for applications such as breathing monitoring, vital-sign detection, and motion tracking.

In the design of a cantenna for a continuous-wave (CW) Doppler radar, engineers typically use a cylindrical waveguide (a metal can) to support the dominant TE_{11} mode, providing a highly directional and stable radiation pattern with well-defined phase center, which is critical for micro-Doppler sensitivity [9]. The waveguide's dimensions are chosen such that the cutoff frequency of

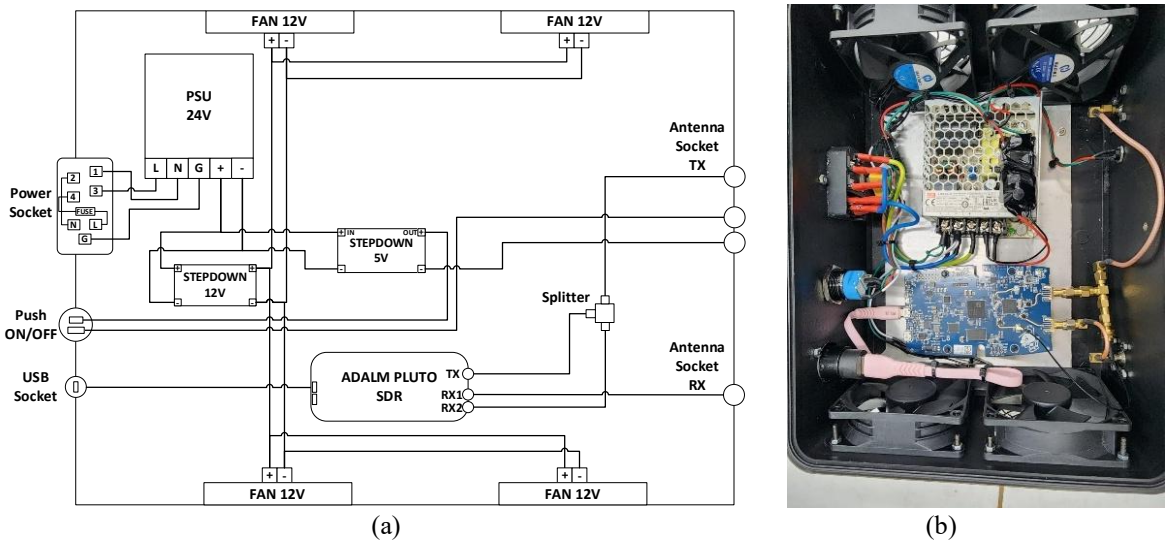

(a) (b)

Figure 3. Hardware of the radar system: (a) design and (b) implementation.

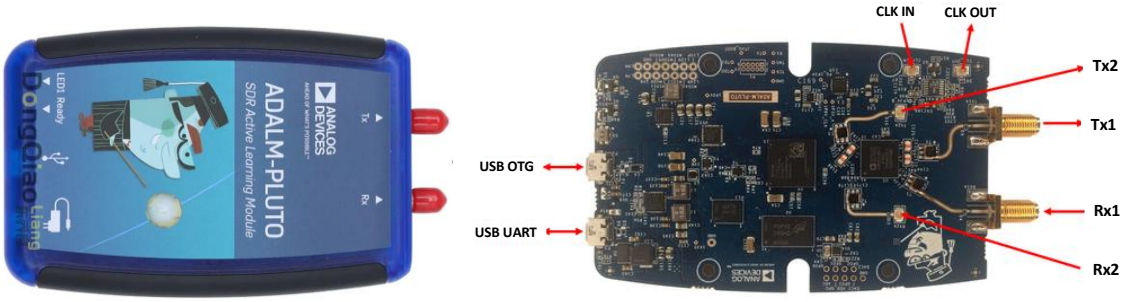

(a) (b)

Figure 4. (a) ADALM-Pluto SDR and (b) Tx1, RX1, RX2 connector.

TE_{11} is just below the transmit frequency, optimizing both gain and mode purity. In practice, the monopole feed is placed a quarter of the internal guide wavelength from the back wall to ensure impedance matching, and the cantenna is integrated into a radar system, demonstrating its ability to measure subtle periodic motions (e.g., pendulum oscillations) via micro-Doppler signatures [10].

1) Cantenna Design and Implementation

The cantenna antenna is designed to operate at 2.45 GHz. This frequency is chosen because it lies within the unlicensed ISM band, making it suitable for research, and because measurement-supporting equipment for this band is available in the laboratory. In addition, its wavelength of 12.24 cm is easy to remember, simplifying antenna design and calculations.

The antenna uses a metal can with a diameter of 8.5 cm. A copper wire 31.2 mm long and 1 mm in diameter serves as the antenna probe and is inserted into the can at a distance of 70 mm from the closed bottom surface (Figure 5 (a)). Figure 5 (b) shows the implementation results.

The design process involves calculating the probe position to achieve a 50 Ω impedance that matches the SDR device and minimizes power loss due to mismatch. Simulations were carried out using CST Studio to ensure optimal radiation pattern and gain.

Antenna simulations were performed to verify parameters such as radiation pattern, gain, VSWR, and antenna efficiency. In the simulation, a can with an 8.5 cm diameter produced a focused radiation pattern with a gain of approximately 8–12 dB, making it suitable for phase-sensitive radar applications.

2) Cantenna Evaluation

The antenna performance was evaluated to verify its radiation characteristics, impedance matching, and efficiency. Key parameters such as Voltage Standing Wave Ratio (VSWR), Return Loss, Distance-To-Fault (DTF) VSWR, and radiation pattern were measured using a Vector Network Analyzer (VNA). Two cantennas were tested, and VSWR values were recorded for both. The ideal VSWR is 1:1, indicating perfect impedance matching; values below 2:1 are generally acceptable. The VSWR readings indicate acceptable values for both antennas, implying low reflected power and good transmission efficiency.

Return loss measurements showed a minimum of -18.29 dB at 2.374 GHz for Antenna 1 and -10.86 dB at 2.416 GHz for Antenna 2. Since return loss values below -10 dB indicate good impedance matching, both antennas met performance expectations. Additionally, DTF VSWR results were 1.78 and 1.52 for Antenna 1 and 2, respectively, confirming low signal reflection along the transmission line.

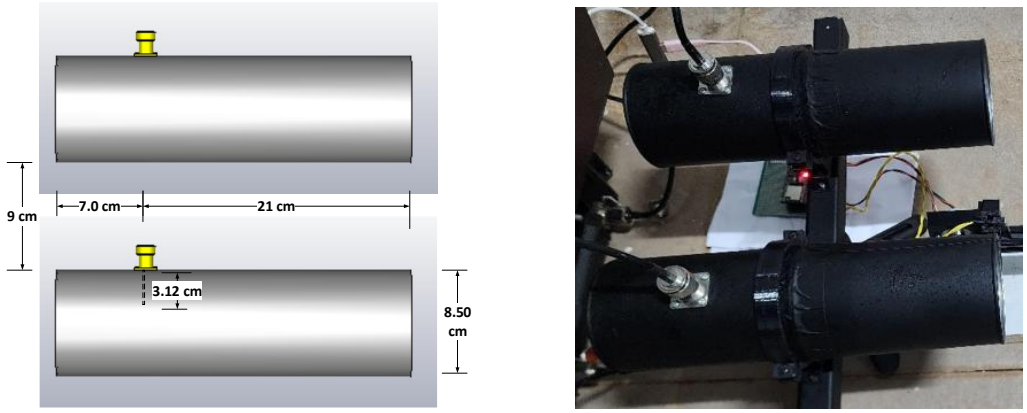

(a) (b)

Figure 5. Cantenna: (a) design and (b) implementation.

TABLE 1
COMPARISON OF VSWR, RETURN LOSS, AND DTF MEASUREMENTS FOR TWO CANTENNA

Parameter	Antenna 1	Antenna 2
Minimum RL Frequency (GHz)	2.374	2.416
Minimum VSWR	1.29	1.48
Return Loss (dB)	-18.29	-10.86
Cable Length (DTF)	3.4909 m	3.5308 m
VSWR (DTF)	1.78	1.52
Radiation Efficiency (%)	~98.52%	~91.77%

The comparative results of cantenna 1 and cantenna 2 for VSWR, return loss, and DTF are summarized as follows (Table 1).

Radiation pattern testing was performed by rotating the cantenna through angles from 0° to 360° in both H-plane and E-plane. The power levels received at each angle were normalized and plotted to form polar diagrams. The resulting plots confirmed the directional radiation characteristic of the cantenna, validating its suitability for focused radar signal transmission.

As shown in Figure 6 (H-plane) and Figure 7 (E-plane), the radiation patterns demonstrate that the cantenna exhibits directional behavior. In the H-plane, the radiation spread is broader horizontally, whereas in the E-plane, the pattern is narrower and more focused. This is consistent with the fundamental properties of the cylindrical open-ended waveguide structure of the cantenna, which naturally directs energy forward while suppressing radiation from the rear. Such radiation characteristics support the use of cantenna in radar systems and point-to-point communication applications where focused beam direction and minimal interference from other directions are essential.

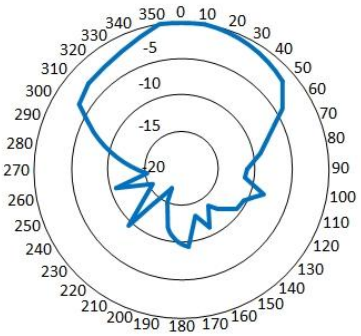

Figure 6. Radiation pattern (H-plane).

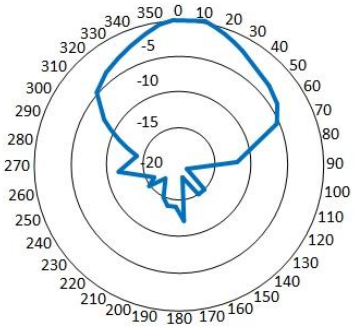

Figure 7. Radiation pattern (E-plane).

E. Motorized Linear Translation Stage

Several studies in high-precision phase-sensitive radar systems employ motorized linear translation stages to accurately control target displacement, enabling sub-millimeter or even micrometer-level phase evaluation. Schulz *et al.* present a 1-THz photonic continuous-wave phase-sensitive radar in which the reflective target is mounted on a motorized stage, allowing controlled positioning during system characterization. Their setup demonstrates outstanding displacement precision, confirming the importance of mechanically guided linear motion for validating radar phase sensitivity [11]. Saqueb *et al.* utilize a motorized linear stage integrated into a rail-based THz synthetic aperture radar (SAR) system to scan an object across the imaging aperture. The controlled linear motion ensures accurate spatial sampling, which is fundamental to reconstructing coherent phase-based SAR images [12]. Meanwhile, Liu *et al.* investigate high-precision motion compensation for THz ISAR imaging, emphasizing that micro-displacements of the target along a linear axis introduce phase migration errors that must be corrected algorithmically. Although not stated explicitly in a single sentence, this type of motion is commonly induced and examined using a precision motorized linear translation stage in experimental ISAR setups [13]. Collectively, these works illustrate that controlled linear translation, typically achieved through motorized stages, is essential for evaluating phase behavior, calibrating displacement sensitivity, and performing coherent imaging in advanced radar systems.

1) Implementation

The implemented motorized linear translation stage consists of a stepper motor connected to a belt-driven slider mounted on an aluminum guide rail, providing stable and controlled linear motion (Figure 8 (a)).

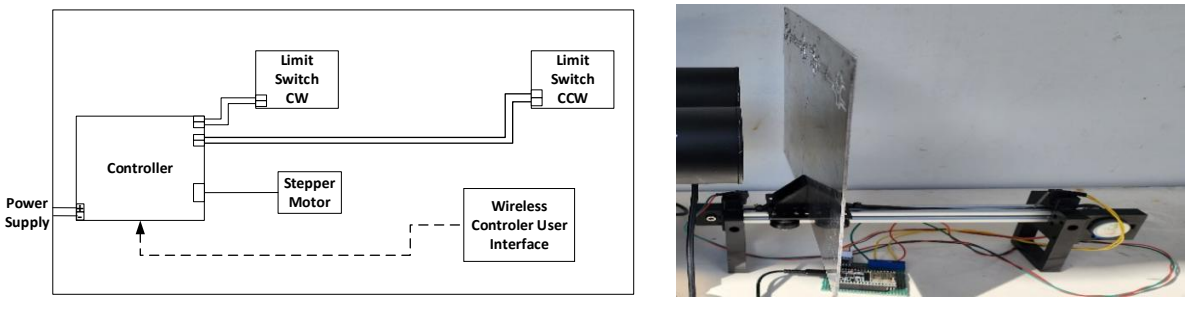

(a) (b)

Figure 8. Motorized linear translation stage: (a) design and (b) implementation.

Figure 9. Controller user interface.

The motor's microstepping control enables fine incremental positioning, while the aluminum structure and guided slider minimize mechanical vibration and lateral play (Figure 8 (b)).

A dedicated controller circuit interfaces with a wireless Android-based remote control system (Figure 9), allowing the user to configure motion parameters, such as forward or reverse direction, step distance, and manual or automatic operation, without physically touching the mechanical assembly. This wireless control approach ensures that the system remains stable and free from external disturbances during adjustment, allowing precise and repeatable displacement of the target platform for measurement and experimentation.

2) Linear Translation Stage Evaluation

The evaluation of the constructed system demonstrated that the mechanical stage successfully translated the aluminum plate target with consistent 0.5 mm step increments in both forward and reverse directions. The motion could be controlled to stop automatically when reaching predefined minimum and maximum limit positions, ensuring safe operation and preventing overtravel.

Additionally, the stage was capable of performing continuous automated reciprocating motion, repeatedly moving back and forth along the translation axis without loss of positioning accuracy. These results confirm that the system provides reliable, repeatable displacement control suitable for phase-sensitive radar measurements.

F. System Integration

The hardware implementation consists of a compact radar unit based on the ADALM-Pluto SDR, along with a splitter, power supply, antenna connectors, and USB interface for communication with a host computer. Two cantenna antennas serve as the transmitter and receiver to provide directional gain and reduce interference (Figure 10).

To enable precise and stable measurement conditions, a motorized linear translation stage with a microstepping drive is integrated, along with a dedicated Android-based wireless controller that allows the user to adjust object positioning parameters without physically disturbing the mechanical setup. The radar signal processing is executed on the computer using a GNU Radio flowgraph specifically designed for phase-sensitive detection.

System evaluation indicates that the overall operation of the radar setup has been successfully verified (Figure 11 (a) and 11 (b)), even though detailed resolution measurements will be carried out in the next stage of testing. The hardware unit operates properly when powered on, as shown by the activation of the cooling fan and the presence of stable regulated outputs from the power supply module. The user has been able to create and execute the GNU Radio flowgraph on the ADALM-Pluto SDR without issue, and the motorized linear translation stage can be operated smoothly. Furthermore, wireless control using the specialized Android remote interface functions reliably, enabling parameter adjustments without disturbing the mechanical setup.

G. Radar Software Design and Implementation

The software radar system is realized in GNU Radio via a flowgraph. The flowgraph development stage accommodates the derivation steps of the equations previously presented in the Theoretical Background subsection.

1) Implementation

The flowgraph consists of the following major blocks, as shown in Figure 12:

- Signal Source block to implement the sine signal generator. It is used to produce the baseband sine wave.

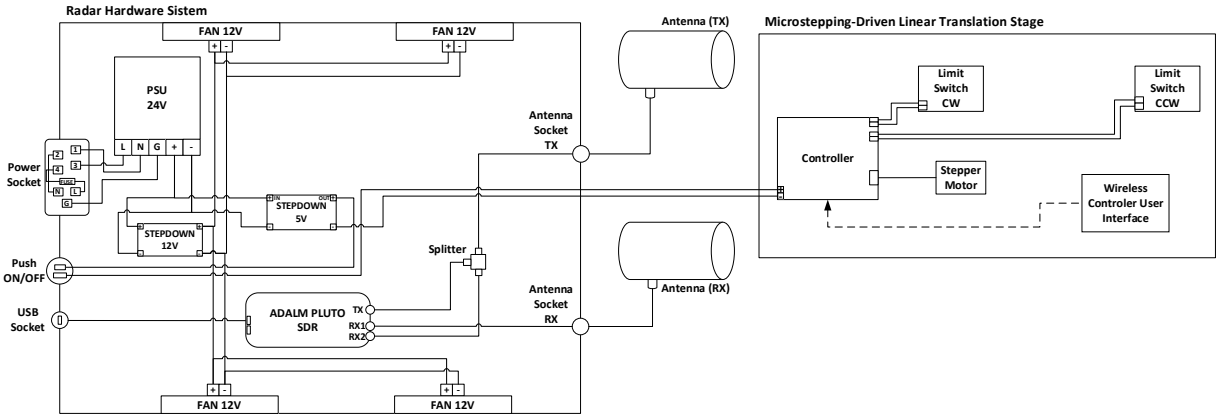

Figure 10. Radar system integration diagram.

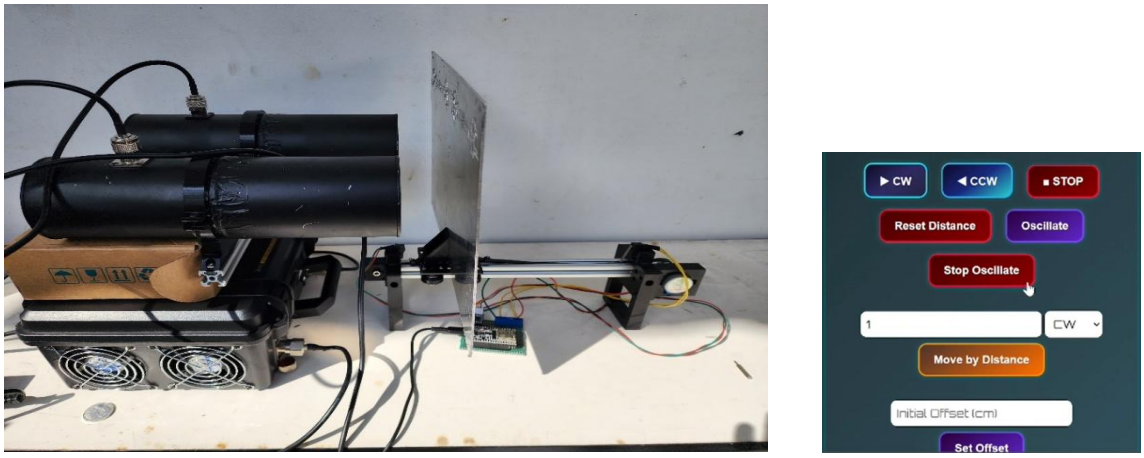

(a) (b)

Figure 11. Proposed radar system integration.

- FMCOMMS2/3/4 Sink block to implement the upconversion process at 2.45 GHz.
- FMCOMMS2/3/4 Source block to implement the downconversion process to recover the baseband signal.
- Multiply Conjugate block to mix the reflected signal with the reference signal in order to obtain the phase difference (in complex form).
- Low-Pass Filter block to implement LPF3; it isolates the baseband reflection.
- Complex to Arg block to determine the phase-difference value in real-number form.
- Moving Average block to calculate the averaged phase value.
- QT GUI Time Sink (Phase Difference) block to visualize the phase-difference signal in the time domain.
- QT GUI Time Sink (Phase Average) block to visualize the averaged phase-difference value numerically.

2) Software Evaluation

This flowgraph has been successfully tested and compiled without errors, indicating that the software is ready to be integrated into the overall radar system.

H. Radar Testing

The testing of the proposed radar involves both hardware and software evaluation (Figure 13). The forward and backward displacement of the object (aluminum plate) is clearly visible. Likewise, the differential phase plot, the averaged phase plot, the numerical phase values, and the phase values shown on the slider all vary in accordance with the small movements of the object. Therefore, it can be concluded that everything is functioning properly.

III. Displacement and Phase Measurements

The general procedure for measuring displacement and phase is to place the object at a certain distance in front of the antenna cylinder and manually record its phase value in a table. The object is then moved farther from the antenna in fixed steps using the previously described motorized linear translation stage. The phase

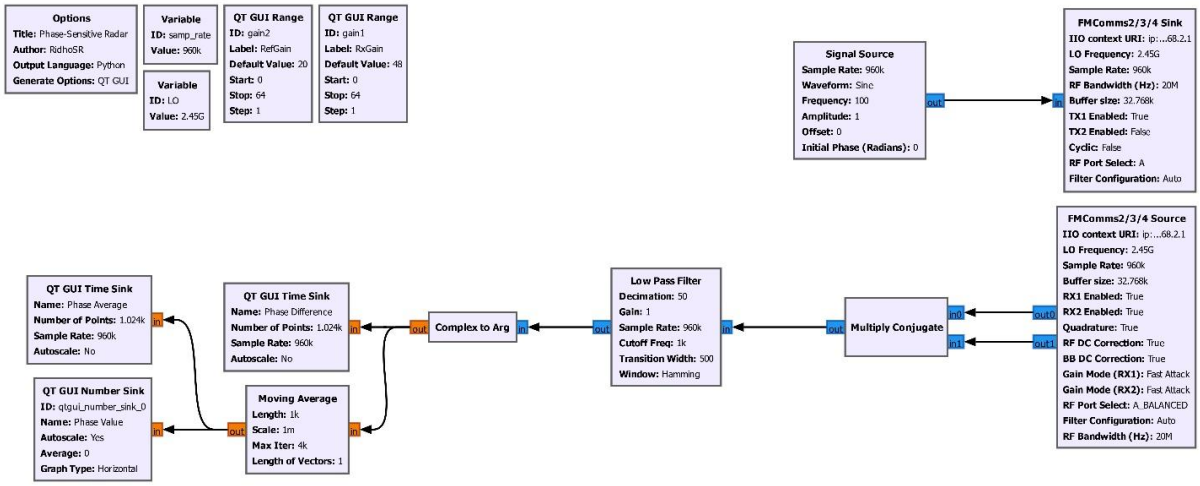

Figure 12. Flowgraph of proposed radar.

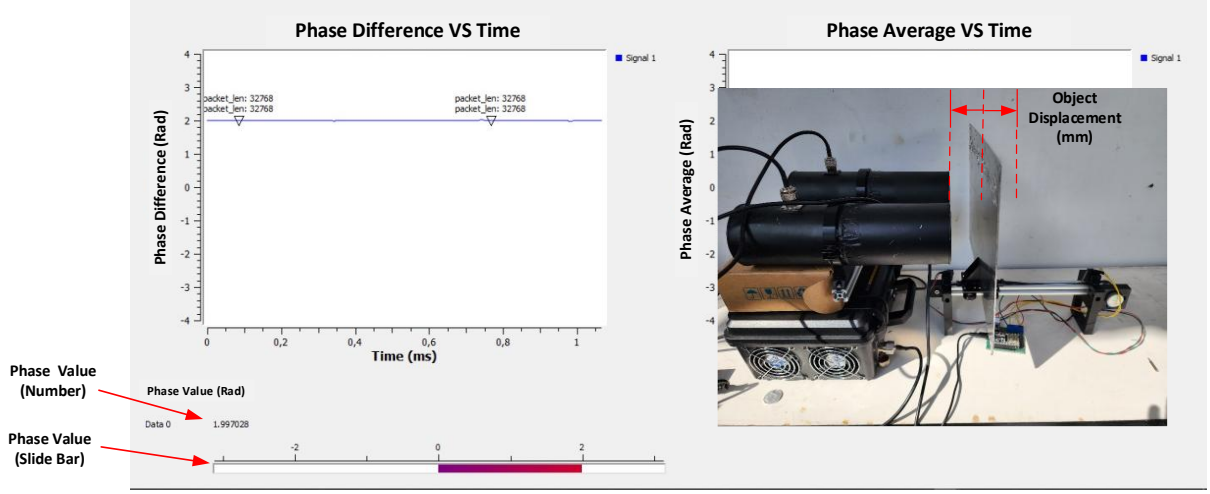

Figure 13. Radar testing.

value is recorded again, and this process is repeated until the desired distance range is reached. The motorized linear translation stage is also used to ensure that the object does not wobble during movement and that each step distance remains consistent.

Because automatic phase logging was not available, the recording had to be done manually by writing down each measured phase value one by one in the table.

Figure 14 shows an example of a measurement at a distance of 26.4 cm, where the obtained Phase Value is 1.997028 rad. This value is also visually represented using a slider bar.

1) *Coarse and Fine Measurements*

Two types of measurements were carried out: coarse measurements and fine measurements. The purpose of the coarse measurement is to obtain a rough overview of the resulting curve and to determine the phase repetition distance. Meanwhile, the fine measurement aims to examine the linearity of the resulting curve and to determine the displacement resolution.

2) *Selection of Step Distance*

Since theoretically we already know that phase repetition occurs every half wavelength, 6.12 cm at 2.45 GHz, the coarse measurement step was set to 1 cm. With this step size, six phase values are obtained for each half-wavelength interval, which is sufficient to roughly observe the shape of the resulting curve. For this measurement, the distance range from 21 cm to 50 cm was selected. The 21 cm point represents the distance from the antenna probe to the front opening of the cantenna, while 50 cm is assumed to be the maximum distance at which the reflected signal can still be detected.

For the fine measurement, a step size of 0.5 mm was chosen because the forward–backward movement range of the target application is 10 mm. Thus, by sampling every 0.5 mm, twenty phase values will be obtained, which is sufficient to construct a non-contact respiratory monitoring application.

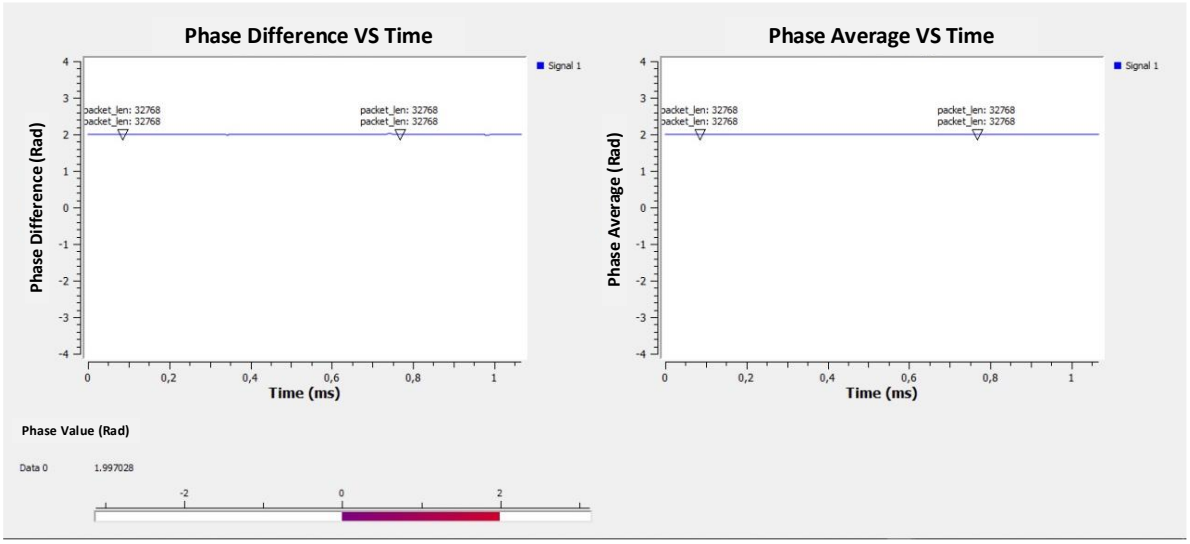

Figure 14. Measurement of phase vs displacement.

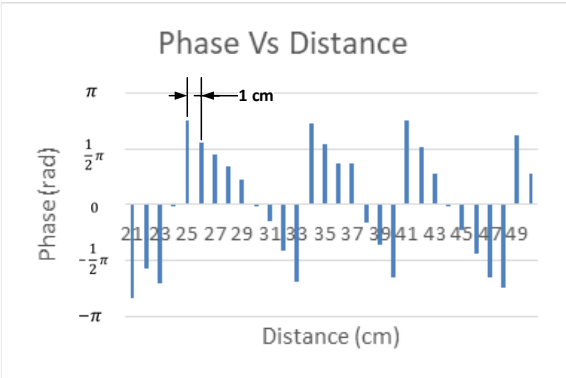

Figure 15. Phase versus distance graph (21-50 cm).

IV. Results

A. Coarse Measurement Results (in 1 cm steps)

Table 2 shows the coarse phase measurement data for distances from 21 to 50 cm. The plotted graph of these coarse measurement results is presented in Figure 15.

From these coarse measurement results, phase repetition is observed at distances of 25 cm, 34 cm, and 41 cm (Figure 15).

B. Fine Measurement Results (in 0.5 mm steps)

The fine measurement with a 0.5 mm step size was carried out in two stages. Stage 1 covered distances from 244.8 to 318.8 mm, and Stage 2 covered distances from 319.3 to 392.8 mm. The total number of manual measurements taken was 2×148 = 296 samples. Due to the large number of samples, the fine measurement data table cannot be presented as was done for the coarse measurement. Therefore, only the resulting curve is shown. Figure 16 presents the phase versus distance graph for the range of 244.8–318.8 mm, while Figure 17 shows the graph for the range of 319.3–392.8 mm.

V. Discussion

The curves obtained from both the coarse measurement (Figure 15) and the fine measurements (Figures 16 and 17) show results consistent with theory. The resulting curve, which appears as a downward-sloping sawtooth, corresponds to the negative sign in (36) (a positive sign would produce an upward-sloping curve).

Table 2
Phase Difference Measurements Corresponding to Object Distance

Distance (cm)	Phase (rad)
21	-3.369940
22	-2.30522
23	-2.84152
24	-0.07206
25	3.035867
26	2.259761
27	1.819484
28	1.387173
29	0.929497
30	-0.00467
31	-0.56372
32	-1.63912
33	-2.75329
34	2.950637
35	2.169441
36	1.514471
37	1.514471
38	-0.64087
39	-1.45257
40	-2.59425
41	3.019974
42	2.091054
43	1.139802
44	-0.05517
45	-0.89318
46	-1.73774
47	-2.58191
48	-2.96489
49	2.510353
50	1.130422

The curve clearly shows phase repetition at every distance interval of $\lambda/2$.

A. Phase Periodicity

The phase–distance measurements exhibit periodic phase wrapping, but the measured repetition distances differ between the coarse and fine experiments. In the first measurement (21–50 cm, 1 cm steps) (Figure 15), the phase repeats approximately every 8 cm, while the high-resolution measurement (244.8–391.8 mm, 0.5 mm steps) (Figure 16 and Figure 17) shows a repetition interval of 73.5 mm. Theoretically, for a 2.45 GHz

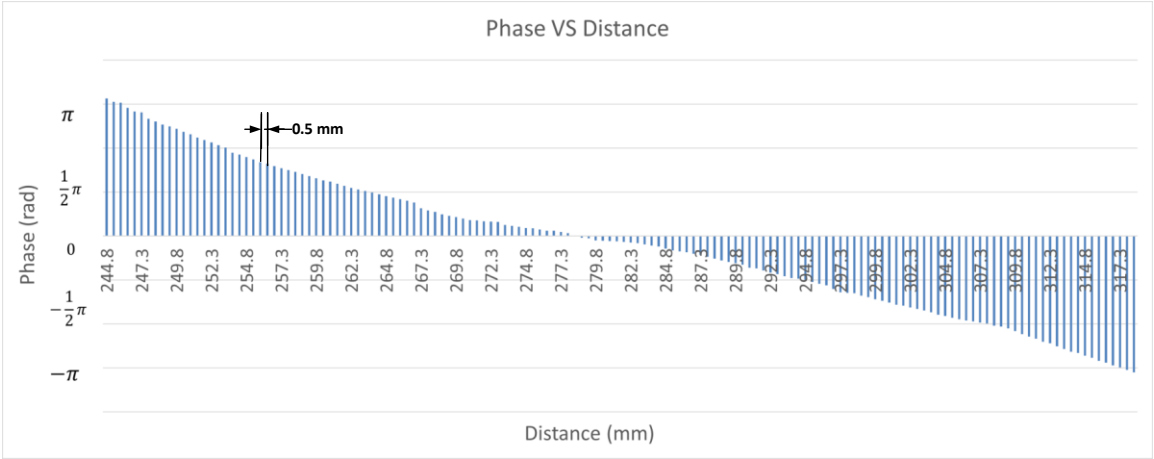

Figure 16. Phase versus distance graph (244.8 mm - 317.3 mm).

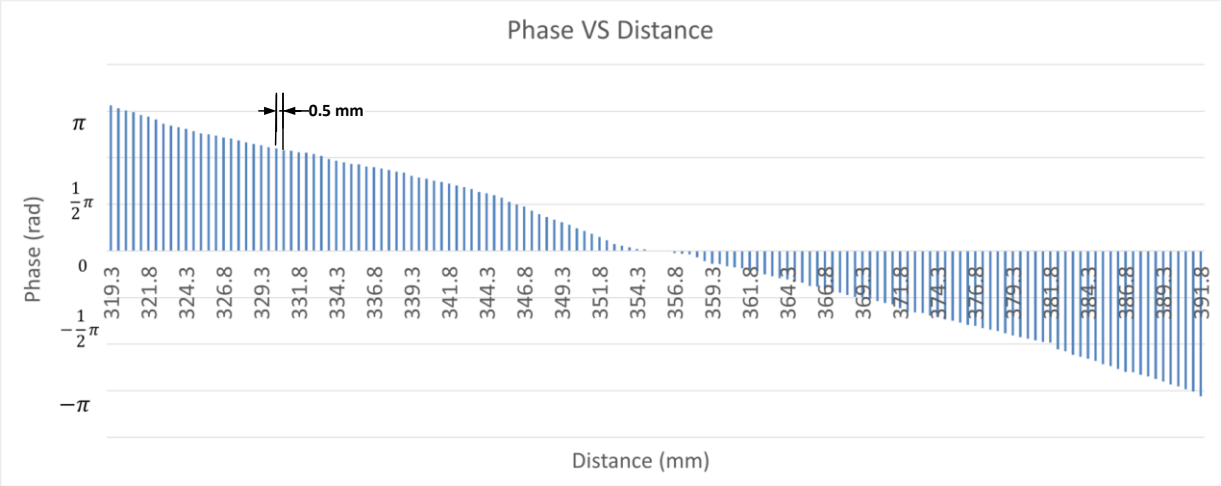

Figure 17. Phase versus distance graph (319.3 mm - 391.8 mm).

continuous-wave radar, the phase should repeat every λ/2 = 61.2 mm.

The deviation observed in the coarse measurement (80 mm vs. theoretical 61.2 mm) is likely caused by phase undersampling and the limited resolution of the 1-cm stepping, which may cause aliasing and masking of the true periodicity. The finer 0.5-mm measurement produces a repetition distance of 73.5 mm, which is significantly closer to the theoretical value but still shows a measurable discrepancy. This residual error may arise from mechanical inaccuracies, environmental multipath, LO phase noise, or imperfect calibration of the reference phase.

Overall, the fine-resolution measurement confirms the expected phase-wrapping behavior, though small systematic offsets remain. These results indicate that the radar's phase sensitivity is functioning correctly, but further calibration or noise suppression may be needed to achieve full theoretical accuracy.

1) Absolute error (bias) of repetition distance

- Definition: measured value minus theoretical value (units: mm).
- Theoretical repetition distance (for 2.45 GHz): λ/2 = 61.2 mm.
- Coarse measurement (21–50 cm, 1 cm step): measured 80.0 mm.
- Absolute error = 80.0 − 61.2 = +18.8 mm.
- Fine measurement (244.8–391.8 mm, 0.5 mm step): measured 73.5 mm.
- Absolute error = 73.5 − 61.2 = +12.3 mm.

2) Relative error (percentage)

- Definition: (absolute error/theoretical) × 100%.
- Coarse: +30.72% (≈30.7%).
- Fine: +20.10% (≈20.1%).

3) Systematic bias (recommended label in discussion)

- Description: the consistent positive offset of measured repetition distances relative to theory (both measurements > λ/2), this indicates a systematic bias rather than purely random noise.
- Report as: "Measured repetition distance shows a systematic positive bias of +18.8 mm (30.7%) for coarse sampling and +12.3 mm (20.1%) for fine sampling."

4) Potentially relevant uncertainty terms

- Spatial sampling (undersampling) error/aliasing, important for the coarse sampling (1 cm steps).
- Mechanical positioning error-stepper inaccuracies, backlash, or repeatability.
- Frequency offset/wavelength calibration error-transmitter/LO frequency not exactly 2.45 GHz.
- Multipath/propagation bias-reflections that change effective path length.
- Phase noise and LO drift-causes phase measurement bias/noise.
- Measurement noise (random)-SNR-limited phase jitter.
- Phase unwrapping/cycle counting error.
- Near-field effects/antenna phase center shift.
- Target not acting as a point reflector.
- Uncalibrated cable/analog group delay.
- Unit conversion or scale misreading.

B. Maximum Detectable Range for Reliable Phase Extraction

In this experiment, the phase–distance curve remained stable and periodic up to approximately 50 cm (Figure 15). Beyond this point, the phase response became noisy, indicating that the maximum range for reliable phase extraction is about 0.5 m.

C. Phase and Displacement Sensitivity

The phase sensitivity and displacement sensitivity of a phase-sensitive radar are intrinsic system parameters determined by the radar's operating wavelength. These quantities can be calculated directly from theoretical relationships without experimental measurement. However, the actual achievable resolution in phase and displacement must be experimentally verified, as it depends on noise, phase stability, and hardware nonlinearity. Displacement and range sensitivity is the same parameter however phase sensitivity and displacement sensitivity are reciprocal quantities.

$$S_\phi = \frac{1}{S_R} = \frac{4\pi}{\lambda} \quad (38)$$

At a radar frequency of 2.45 GHz, where $\lambda = 0.1224$ m, Phase Sensitivity,

$$S_\phi = \frac{4\pi}{\lambda} = 102.7 \text{ rad/m} = 0.1027 \text{ rad/mm}$$

and Displacement Sensitivity:

$$S_R = \frac{1}{102.7} = 0.00974 \text{ m/rad} = 9.74 \text{ mm/rad}$$

D. Displacement Resolution

In this study, we successfully generated measurement curves with a 0.5 mm step size (Figures 16 and Figure 17). From these graphs, it is clearly observed that a 0.5 mm displacement still produces noticeable changes in the curve, confirming that the radar is capable of achieving a 0.5 mm displacement resolution.

However, this resolution has not been fully characterized, and it is likely that the actual achievable resolution is below 0.5 mm if further measurements were conducted. Such measurements were not performed because using a step size smaller than 0.5 mm would require substantial effort, particularly in data recording, which in this study is still carried out manually. Additionally, the mechanical translation system would need to be extremely stable and precise. Therefore, this will be addressed as a topic for future research.

E. Linearity

Linearity refers to how closely the measured phase response follows a straight-line relationship with respect to the target displacement or distance. From the graphs in Figure 16 and Figure 17, it can be seen that, in general, the curves exhibit a linear tendency consistent with theory (see the phase–distance equation in the Theoretical Background subsection). However, in several portions, particularly in the range of 244.8–279.8 mm, significant deviations can be observed. This occurs because the object is positioned very close to the antenna, approximately 4.5 cm away. Other contributing factors to the nonlinearity are the same as those discussed in the Phase Periodicity section.

F. Comparison between Phase-Sensitive Radar Using SDR ADALM-Pluto and Conventional Radar Systems

As presented in Table 3, phase-sensitive radar implemented using Software Defined Radios (SDRs), such as the ADALM-Pluto, offers high flexibility, reconfigurability, and low cost, making it attractive for research and rapid prototyping. However, its performance is limited by low transmit power, restricted bandwidth, and moderate phase stability, resulting in lower phase sensitivity and higher noise.

In contrast, conventional phase-sensitive radars employ dedicated high-quality RF hardware with wide bandwidth and highly stable oscillators, enabling superior displacement resolution, higher SNR, and more accurate phase tracking.

Consequently, SDR-based systems are ideal for experimentation and algorithm development, while conventional systems are better suited for applications requiring high precision, long-term stability, and robust detection performance.

G. Potential Applications

Assuming that the chest motion during respiratory (Δd_respiration) has a displacement range of approximately 10 mm [14], and the proposed radar achieves a displacement resolution of 0.5 mm, there will be about 20 distinct phase samples representing the corresponding distance changes. This dense phase sampling enables the respiratory signal to be clearly visualized in the form of a displacement graph and accurately converted back into the distance domain. Consequently, the proposed radar shows strong potential for non-contact respiratory monitoring application, as shown in Figure 18, particularly because the fine displacement resolution allows the system to capture small yet critical chest movements. Furthermore, the large number of phase samples obtained within a single breathing cycle enhances robustness against noise and facilitates the use of smoothing algorithms and respiratory feature extraction techniques.

H. Proposed Future Work

Although the developed phase-sensitive radar system based on the ADALM-Pluto has successfully demonstrated a displacement resolution of 0.5 mm, several research directions remain open to further improve performance, robustness, and applicability. The following points outline the recommended next research steps.

TABLE 3
PERFORMANCE COMPARISON BETWEEN SDR-BASED AND CONVENTIONAL PHASE-SENSITIVE RADARS

Parameter	SDR-Based Phase-Sensitive Radar	Conventional Phase-Sensitive Radar
Frequency	Flexible (325 MHz–3.8 GHz)	Fixed (2.4, 5.8, 10, 24 GHz, etc.)
Bandwidth	Limited (5–20 MHz)	Wide (100 MHz–1 GHz+)
Range Resolution	Lower (≈7.5 m @ 20 MHz)	Higher (≈0.75 m @ 200 MHz)
Displacement Resolution	Moderate (≈0.5–1 mm displacement detectability)	High (≈0.1 mm or better)
Phase Stability	Affected by jitter and clock drift	Very stable (low-noise oscillators)
SNR	20–30 dB	40–60 dB
Transmit Power	Very low (~0 dBm)	Much higher (10–40 dBm)
Maximum Range	Short (0.3–1.5 m typical)	Long (1–5+ m depending on system)
Flexibility	Very high (waveform, DSP, frequency fully programmable)	Low (fixed hardware)
Cost	Very low (< $200)	High (>$10,000)

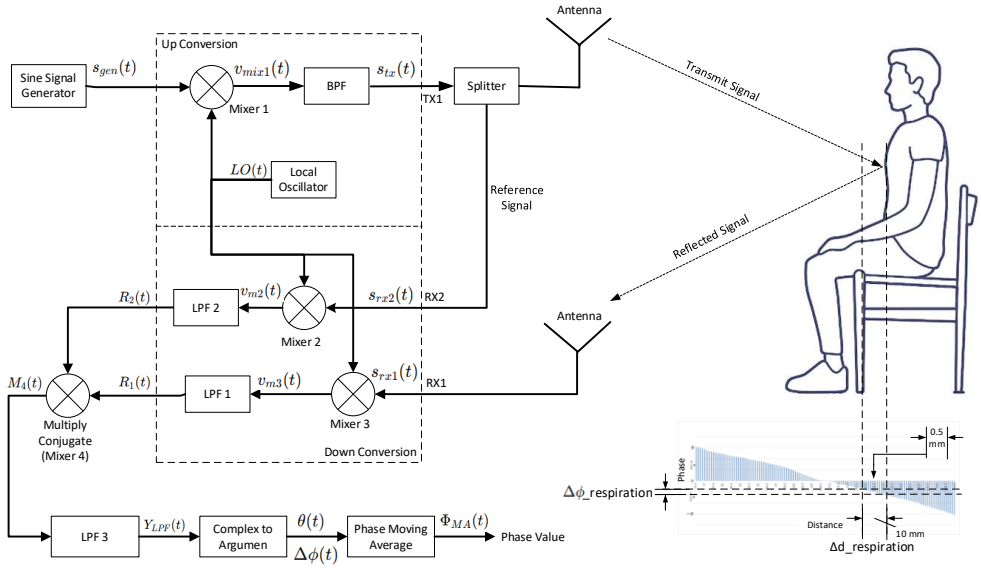

Figure 18. Non-contact human respiratory monitoring application.

1) Automated High-Granularity Displacement Scanning

The current displacement measurement process still relies on manual procedures, stepping the target by 0.5 mm using a stepper motor, recording the phase values manually, and plotting the results. This approach is time-consuming and limits the achievable resolution. As future work, an automated displacement scanning platform should be developed. This platform would:

- Control the stepper motor with sub-0.5 mm increments (e.g., 0.1 mm or 0.05 mm).
- Automatically synchronize each displacement step with real-time phase acquisition from the radar.
- Store and process all data automatically to eliminate operator-induced delays and errors.

Such automation would allow the true ultimate displacement resolution limit of the radar to be determined experimentally with high confidence.

2) Investigation of the Fundamental Resolution Limit

Once the automated system is in place, experiments can be conducted to explore:

- The smallest reliably detectable displacement (theoretical vs measured).
- Phase linearity at very small displacement intervals.
- Noise sensitivity and the minimum signal-to-phase-conversion threshold.

This study will clarify whether the radar can surpass 0.5 mm resolution and approach the theoretical bound determined by wavelength, SNR, and hardware stability.

3) Real-Time Phase Unwrapping and Drift Compensation

At small displacement steps (<0.5 mm), phase noise and system drift become significant. Future work should include:

- Implementing real-time phase unwrapping algorithms to maintain tracking stability.
- Designing phase drift compensation using reference reflectors, temperature monitoring, or PLL-based correction.
- Applying digital filtering (e.g., Kalman filter, adaptive filtering) to isolate true movement from phase jitter.

This will improve measurement reliability for both static calibration and dynamic motion monitoring.

4) Integration With Real-World Motion Monitoring

After the system's fine-resolution capabilities are established, the next step is to evaluate the radar in real applications such as:

- Respiratory and heartbeat monitoring.
- Micro-vibration detection of mechanical structures.
- Animal motion monitoring, especially small chest movements or subtle behavioral indicators.
- Human–computer interaction based on micro-gestures.

These applications require stable detection of sub-millimeter motion, making them ideal benchmarks for the mature system.

5) Development of Multi-Frequency or Wideband Operation

To extend range and reduce ambiguity:

- Explore multi-tone or FMCW techniques using the same ADALM-Pluto.
- Combine phase radar (for fine displacement) with range radar (for object localization).
- Evaluate whether using multiple frequencies improves phase stability or reduces environmental sensitivity.

This hybrid approach may enhance both resolution and robustness.

6) Environmental Robustness Characterization

Future research should quantify the influence of:

- Temperature variations.

- Multipath and indoor clutter.
- Different target reflectivity.
- Human presence or movement near the test setup.

This will help determine how the radar performs under realistic field conditions and lead to guidelines for calibration or compensation.

7) Software Tools for Automatic Analysis

Another important direction is to build a software framework that performs:

- Automatic phase extraction.
- Regression, linearity analysis, and sensitivity estimation.
- Generation of resolution, noise, and drift reports.
- Real-time visualization during measurements.

This will make the system more user-friendly, reproducible, and suitable for long-term experiments.

VI. CONCLUSION

This study demonstrated the development of a phase-sensitive radar system using ADALM-Pluto SDR and a cantenna operating at 2.45 GHz. The system successfully detected sub-millimeter displacements by analyzing phase shifts between transmitted and reflected CW signals. The system exhibited a clear, near-linear phase-distance relationship, with displacement resolution to sub-millimeter changes. The directional cantenna showed high efficiency, reinforcing the radar's precision. Although, smallest reliably detectable displacement (theoretical vs measured) was not defined, displacement resolution testing confirmed the system's capability to detect movements as small as 0.5 mm. The demonstrated 0.5-mm displacement resolution confirms that the proposed radar can effectively detect subtle respiratory motions, underscoring its applicability to real-time respiratory monitoring. Future work will focus on automating the displacement measurement process to enable sub-0.5 mm step sizes and eliminate manual data recording. This will allow the true ultimate displacement resolution of the radar to be determined experimentally. Additional research will include real-time phase unwrapping and drift compensation, environmental robustness analysis, multi-frequency operation to enhance performance, and evaluation of the system in real-world micro-motion monitoring applications such as non-contact human respiratory and heartbeat monitoring.

DECLARATIONS

Conflict of Interest

In completing this paper, the authors affirm that no competing interests exist.

CRediT Authorship Contribution

Eril Mozef: Conceptualization, Methodology, Supervision, Formal analysis, Validation, Investigation, Writing-Review and Editing; Ridho Shofwan Rasyid: Data curation, Resources, Software, Writing-Original draft preparation, Funding Acquisition, Project administration; Enceng Sulaeman: Review; Tiyo Rizky Mulyana: Data curation, Software; Fahrizal Al Farik: Data curation; Thaskia Qolbi Junjunan: Software.

Funding

Research reported in this publication was supported by the Final Project Assistance Fund Program, Telecommunication Engineering Study Program, Bandung State Polytechnic, Indonesia.

Acknowledgment

The authors would like to thank PT Solusi Intek Indonesia for providing experimentation facilities for data generation.

REFERENCES

[1] A. D. Droitcour, O. Boric-Lubecke, V. M. Lubecke, J. Lin, and G. T. A. Kovacs, "Range correlation and I/Q performance benefits in single-chip silicon doppler radars for noncontact cardiopulmonary monitoring," *IEEE Trans. Microw. Theory Tech.*, vol. 52, no. 3, pp. 838–848, Mar. 2004, doi: 10.1109/TMTT.2004.823552.

[2] M. S. Raheel *et al.*, "Contactless vital sign monitoring systems: A comprehensive survey of remote health sensing for heart rate and respiration in internet of things and sleep applications," *Sensors & Diagnostics*, vol. 3, no. 7, pp. 1085–1118, 2024, doi: 10.1039/D4SD00073K.

[3] M.-C. Huang, J. J. Liu, W. Xu, C. Gu, C. Li, and M. Sarrafzadeh, "A self-calibrating radar sensor system for measuring vital signs," *IEEE Trans. Biomed. Circuits Syst.*, vol. 10, no. 2, pp. 352–363, Apr. 2016, doi: 10.1109/TBCAS.2015.2411732.

[4] S. Costanzo, "Software-defined doppler radar sensor for human breathing detection," *Sensors*, vol. 19, no. 14, p. 3085, Jul. 2019, doi: 10.3390/s19143085.

[5] U. Saeed, Q. H. Abbasi, and S. A. Shah, "AI-driven lightweight real-time SDR sensing system for anomalous respiration identification using ensemble learning," *CCF Trans. Pervasive Comput. Interact.*, vol. 4, no. 4, pp. 381–392, Dec. 2022, doi: 10.1007/s42486-022-00113-6.

[6] M. Rehman *et al.*, "Enhancing system performance through objective feature scoring of multiple persons' breathing using non-contact rf approach," *Sensors*, vol. 23, no. 3, p. 1251, Jan. 2023, doi: 10.3390/s23031251.

[7] E. Mozef, R. S. Rasyid, and E. Sulaeman, "Program aplikasi RATIFA v.1.0 - radar sensitif fasa berbasis software-defined radio (SDR) ADALM-Pluto dengan antena cantenna," Reg. No. 000902787; App. No. EC002025062526, 2025

[8] C. A. Balanis, *Antenna Theory: Analysis and Design*, 4th ed. Hoboken, NJ, USA: John Wiley & Sons, Inc., 2016.

[9] M. Elhefnawy, "Design and simulation of a doppler-radar RF front-end transceiver," *Adv. Sci. Technol. Eng. Syst. J.*, vol. 4, no. 5, pp. 250–257, 2019, doi: 10.25046/aj040531.

[10] A. Harsh, "Measuring radar signatures of a simple pendulum using cantenna radar," *Int. J. Comput. Technol.*, vol. 15, no. 5, pp. 6785–6795, Apr. 2016, doi: 10.24297/ijct.v15i5.1653.

[11] N. Schulz *et al.*, "High-speed 1 THz photonic continuous wave phase-sensitive radar with micrometer precision," *J. Infrared, Millimeter, Terahertz Waves*, vol. 46, no. 11, p. 76, Nov. 2025, doi: 10.1007/s10762-025-01095-z.

[12] S. A. N. Saqueb, J. L. Garry, G. E. Smith, N. K. Nahar, and K. Sertel, "THz imaging using rail-based synthetic aperture radar for the detection of concealed objects," in *Proc. Usn. Nat. Radio Sci. Meet.*, 2018, pp. 175–176. doi: 10.1109/USNC-URSI.2018.8602878.

[13] W. Liu, H. Wang, Q. Yang, B. Deng, L. Fan, and J. Yi, "High precision motion compensation THz-ISAR imaging algorithm based on KT and ME-MN," *Remote Sens.*, vol. 15, no. 18, p. 4371, Sep. 2023, doi: 10.3390/rs15184371.

[14] H. Kim and J. Jeong, "Non-contact measurement of human respiration and heartbeat using W-band doppler radar sensor," *Sensors*, vol. 20, no. 18, p. 5209, Sep. 2020, doi: 10.3390/s20185209.